Essay

Convolution Power Ratio Based on Single-Ended Protection Scheme for HVDC Transmission Lines

Guangqiang Peng [1], Lixin Chen [1], Jiyang Wu [1], Huimin Jiang [2], Zhijie Wang [2] and Haifeng Li [2,*

[1] Electric Power Research Institute of EHV, Guangzhou 510633, China; pengguangqiang@ehv.csg.cn (G.P.); chenlixin@ehv.csg.cn (L.C.); wujiyang@ehv.csg.cn (J.W.)

[2] School of Electric Power Engineering, South China University of Technology, Guangzhou 510641, China; 202311082961@mail.scut.edu.cn (H.J.); 202311083086@mail.scut.edu.cn (Z.W.)

* Correspondence: lihf@scut.edu.cn

Abstract: In order to solve the problems of insufficient abilities to withstand transition resistance under remote faults and difficulties in identifying internal and external faults for HVDC transmission line protection, a new single-ended protection scheme based on time-domain convolutional power was proposed. In this scheme, the ratio of time-domain convolution power at different frequencies is used to detect internal and external faults, and the long window convolution power is used to form the pole selection criteria. Due to the integration of transient power fault characteristics at high and low frequencies, this scheme amplifies the characteristic differences between internal and external faults caused by DC line boundaries and has a strong ability to withstand transition resistance. Based on PSCAD/EMTDC, simulation verification was conducted on the Yunnan–Guangzhou ±800 kV HVDC project. The results show that the proposed single-ended protection scheme can effectively identify fault poles, as well as internal and external faults. It has strong resistance to transition resistance and certain anti-interference ability and has strong adaptability to DC line boundaries, which meets the protection requirements of HVDC transmission systems for high speed, selectivity and reliability.

Keywords: convolution power; direct current boundary; high voltage direct current transmission; line protection

1. Introduction

Due to remarkable advantages such as lower construction costs, lower losses and bulk and long-distance power transmission capabilities, line-commutated converter high-voltage direct current (LCC-HVDC) systems are widely used [1–4]. The transmission line is the component with the highest fault probability, and line faults affect the whole HVDC system. Therefore, the rapid removal of faults is crucial to the enhancement of the transient stability of power systems [5–8]. Currently, fault identification methods for HVDC transmission lines can be summarized into the following two schemes:

Time domain characteristics based on methods: Traditional time domain schemes typically utilize the transient characteristics of voltage traveling wave attenuation caused by boundaries composed of smoothing reactors at both ends of the line, such as traditional methods of voltage change rate [9,10]. These methods are simple and have low computational complexity and are widely used in practical engineering. However, they will significantly decrease with an increase in transition resistance, thereby affecting the sensitivity of protection. Ref. [11] uses the method of integrating the sum of positive and negative limit current reactance voltages to identify internal and external faults, which has strong anti-noise interference ability and is not affected by AC measurement faults; however, the scheme has a weak ability to withstand transition resistance, and it is easy to misjudge when high-impedance grounding faults occur at the end of the line.

Compared with the above methods based on a certain time domain, utilizing the waveform characteristics of local wave fronts under internal and external faults is also an effective approach. In Refs. [12,13], the Levenberg–Marquardt method was used to fit the initial traveling wave voltage of the measurement point fault, and the failure modes and exponential terms of different fault characteristics were obtained. Reference [14] calculates the concavity and convexity of the current-limiting reactance voltage for fault identification. Reference [15] utilizes a multi-resolution morphological gradient algorithm to extract the polarity information of fault traveling waves, which has low sampling frequency requirements. However, references [12–15] all require correct calibration of the initial fault traveling wave to avoid the influence of reflected traveling waves at the beginning and end of the line. In the event of near-end or terminal faults, the arrival time interval between the first and secondary traveling waves is very short, and there may be significant errors in correctly calibrating the traveling wave within a short time window, resulting in protection malfunction or rejection.

Frequency domain characteristics based on methods: The frequency domain method usually utilizes the high-frequency attenuation of fault traveling waves at the boundaries of DC lines and uses frequency domain extraction tools such as wavelet transforms, and Fourier transforms to extract high-frequency information. Traditional frequency domain extraction methods usually extract transient feature information under a single frequency band. For example, in reference [16], wavelet transforms were used to extract the high-frequency voltage component to identify the faults; reference [17] uses the measured impedance at resonant frequency for fault identification based on the amplitude–frequency characteristics of DC filters. Study [18] extracted the voltage and current data of specific frequency bands on both sides of a reactor, and then calculated the boundary energy to form longitudinal protection. However, the traditional method of extracting a single frequency band has the problem of having poor resistance to transition resistance.

To address the above problems, many methods based on multi-frequency-band transient characteristics are proposed. Reference [19] uses the energy of multiple voltage characteristic frequency bands to construct fault criteria. However, its calculation principle is complex due to voltage energy calculations in multiple frequency bands. The ratios of voltages at different frequency features used in references [20–22] serve as a criterion for fault identification. In [23,24], stationary wavelet transforms and Hilbert–Huang transforms were used to extract the features of multi-frequency-band voltage, which can effectively amplify the characteristic differences of internal and external faults. However, all these methods require higher sampling frequencies and have complex calculation problems.

To improve the above-mentioned problems such as poor resistance and high sampling frequency, a single-ended protection scheme was proposed for high-voltage DC transmission lines based on convolutional power.

1. The differences in the mathematical analytical formulas for transient frequency domain power under internal and external faults in the HVDC transmission line are deduced. Through detailed analysis of the frequency characteristics of faults that are internal and external to the area, it can be concluded that convolutional power is beneficial for amplifying the characteristic differences between internal and external faults to the area caused by the boundary of the DC line.

2. In this study, by introducing the convolutional power in the time domain as the power in the frequency domain, it is proposed that the convolutional power of the short time window is used as the main criterion, and the ratio of the convolutional power of the long and short windows is used as the auxiliary criterion for the identification of high-impedance faults. The two complement each other to realize the fault pole, fault direction and fault identification, internal and external to the area.

3. The proposed scheme can extract high- and low-frequency information without frequency domain extraction tools; the calculation principle is simple; the convolution power ratio at different frequencies is less affected by the transition resistance; and the proposed protection scheme is still adaptable under weak boundary conditions.

2. Analysis of Frequency Domain Characteristics and Influencing Factors

2.1. Frequency Domain Characteristics of Internal and External Faults

Forward faults (FFs) include internal faults and external faults near the inverter side. Taking the line end fault f_1 and the external fault f_2 on the HVDC transmission line in Figure 1 as examples, protection measuring points (M) are installed at the outlet of the rectifier station. The reverse fault (RF) is f_3.
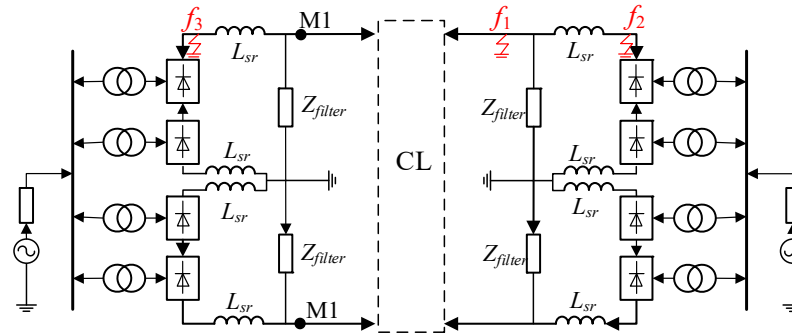

Figure 1. Internal fault and external fault on the HVDC transmission line.

To eliminate the influences of positive and negative pole coupling, the double-pole line is decoupled into a line-model and ground-model network through the Klenberg transform. Moreover, according to Peterson's law and superposition theorem, superimposed circuits for f_1 and f_2 can be obtained for FF, as shown in Figure 2. The black arrow is the current-related direction at M, and the red arrow is the direction of the fault current.
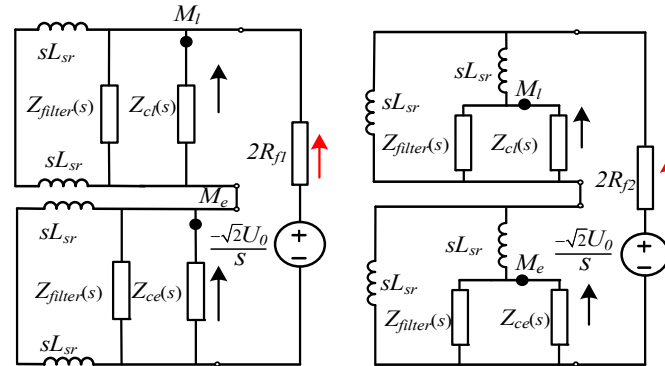

Figure 2. Superimposed circuit of fault point f_1 and f_2.

For Figure 2, the internal equivalent impedance at f_x (x = 1,2) is as follows:

$$Z_{f1k} = Z_{ck}//Z_{filter}//s2L_{sr}(k = l, e) \tag{1}$$

$$Z_{f2k} = (Z_{ck}//Z_{filter} + sL_{sr})//sL_{sr}(k = l, e) \tag{2}$$

where L_{sr} is the current-limiting reactance value on the DC side, $Z_{cx(x=l,e)}$ is the wave impedance of the DC transmission line, $R_{fx(x=1,2)}$ is the transition resistor and U_0 indicates the rated voltage of the line $Z_{filter} = 1/sC_{f1} + sL_{f1} + 1/sC_{f2}//sL_{f2} + 1/sC_{f3}//sL_{f3}$.

Thus, the electrical quantity of the mold network at f_x (x = 1,2) is the following:

$$\begin{cases} U_{fxk}(s) = \dfrac{-\sqrt{2}U_0 Z_{fxk}(s)}{s(Z_{fxl}(s)+Z_{fxe}(s)+2R_{fx})} \\ I_{fxk}(s) = \dfrac{\sqrt{2}U_0}{s(Z_{fxl}(s)+Z_{fxe}(s)+2R_{fx})} \end{cases} (k = l, e) \tag{3}$$

where $U_{fxk(k=l,e)}$ and $I_{fxk(k=l,e)}$ are the voltages and currents of the line mode and zero mode components at the fault locations, respectively.

We determined that the TW at f_2 to M, which needs to be multiplied by a partial voltage coefficient λ_u, is as follows:

$$\lambda_u = \frac{Z_{ck}(s)//Z_{filter}(s)}{Z_{ck}(s)//Z_{filter}(s)+sL_{sr}} (k = l, e) \quad (4)$$

According to (1)–(4), the general expression of fault TW for f_x (x = 1,2) can be obtained at M as follows:

$$\begin{cases} U_{mf1k}(s) = U_{mf1k}(s); U_{mf2k}(s) = \lambda_u U_{mf2k}(s) \\ I_{mf1k}(s) = U_{mf1k}(s)/Z_{ck}(s); I_{mf2k}(s) = \lambda_u U_{mf2k}(s)/Z_{ck}(s) \end{cases} \quad (5)$$

where $U_{mf1k(k=l,e)}$ and $I_{mf1k(k=l,e)}$ are the voltages and currents of the line mode and zero mode components at the measurement point when a fault occurs at f_1, respectively.

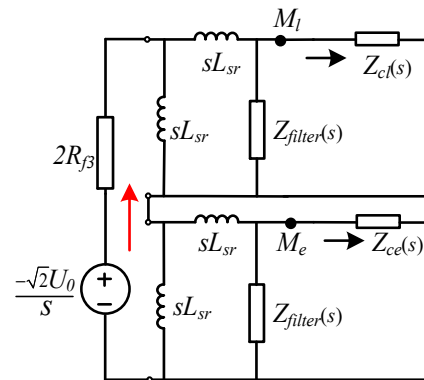For the RF, the superimposed circuit for f_3 outside the rectifier side is shown in Figure 3.

Figure 3. Superimposed circuit of fault point f_3.

Since both ends are on the LCC side, the equivalent impedance at the outlet of the converter station is the same, and the superimposed circuits for f_3 and f_2 are the same, i.e., $Z_{f3k} = Z_{f2k}$. The difference lies in the direction of the fault current. Therefore, the expression of the fault TW at M for f_3 is the following:

$$\begin{cases} U_{mf3k}(s) = \frac{-\lambda_u \sqrt{2} U_0 Z_{f3k}(s)}{s(Z_{f3l}(s)+Z_{f3e}(s)+2R_{f3})} (k = l, e) \\ I_{mf3k}(s) = -U_{mf3k}(s)/Z_{ck}(s) \end{cases} \quad (6)$$

where $U_{mf3k(k=l,e)}$ and $I_{mf3k(k=l,e)}$ are the voltages and currents of the line mode and zero mode components at the measurement point M when the fault occurs at the fault point f_3, respectively.

The convolution in the time domain is equal to the product in the frequency domain [21], the power in the frequency domain corresponding to f_1, f_2, and f_3 can be obtained as follows:

$$P_{mf1k}(s) = U_{mf1k}(s)I_{mf1k}(s) = -\frac{2U_0{}^2(Z_{f1k}(s))^2}{s^2(Z_{f1l}(s) + Z_{f1e}(s)+2R_{f1})^2 Z_{ck}(s)} \quad (7)$$

$$P_{mf2k}(s) = U_{mf2k}(s)I_{mf2k}(s) = -\frac{2U_0{}^2(Z_{f2k}(s)\lambda_u)^2}{s^2(Z_{f2l}(s) + Z_{f2e}(s)+2R_{f2})^2 Z_{ck}(s)} \quad (8)$$

$$P_{mf3k}(s) = U_{mf3k}(s)I_{mf3k}(s) = \frac{2U_0{}^2(Z_{f3k}(s)\lambda_u)^2}{s^2(Z_{f3l}(s) + Z_{f3e}(s) + 2R_{f3})^2 Z_{ck}(s)} \tag{9}$$

where $P_{mf1k(k=l,e)}$, $P_{mf2k(k=l,e)}$ and $P_{mf3k(k=l,e)}$ are the power values of the line mode and zero mode components at the measurement point M when faults occur at f_1, f_2 and f_3, respectively.

To visually evaluate the characteristic differences of different electrical quantities at f_1 and f_2, for $G_U(s) = U_{f2}(s)/U_{f1}(s)$, $G_I(s) = I_{f2}(s)/I_{f1}(s)$ and $G_P(s) = P_{f2}(s)/P_{f1}(s)$, the amplitude–frequency curve is shown in Figure 4.
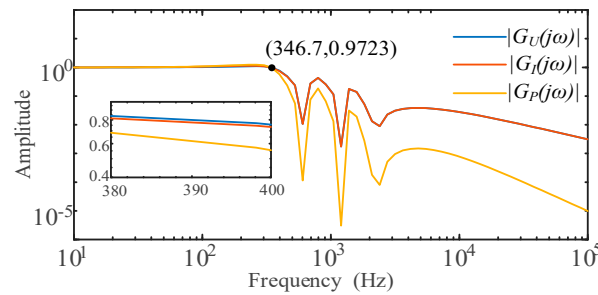
Figure 4. Amplitude-frequency curves of $|G_U(j\omega)|$, $|G_I(j\omega)|$ and $|G_P(j\omega)|$ ($R_{f1} = R_{f2} = 0$).

As a result of the influence of the DC boundary, the above ratios are each less than 1. As shown in Figure 4, the amplitude–frequency curves of $|G_U(j\omega)|$ and $|G_I(j\omega)|$ are very similar, and $|G_P(j\omega)|$ is not as different from these values in the frequency range of 0 to 340 Hz. However, when the frequency is greater than 340 Hz, the $|G_P(j\omega)|$ curve becomes lower than these curves. The gap between $|G_P(j\omega)|$ and either $|G_U(j\omega)|$ or $|G_I(j\omega)|$ increases significantly as the frequency increases. Therefore, in the high-frequency band, the attenuation of the frequency domain power by the DC boundary is more serious than that of a single voltage or current, and the degree of attenuation intensifies as the frequency increases. Hence, compared to using voltage or current alone, $P_{fi}(s)$ can be used to more effectively identify internal and external faults.

2.2. Influencing Factors

The generation of fault TWs is mainly affected by three factors: dispersion, refraction and reflection and fault resistance.

2.2.1. The Dispersion of Traveling Waves

As traveling waves propagate, fault decay due to the influence of long-distance transmission lines occurs, as shown in Figure 5.
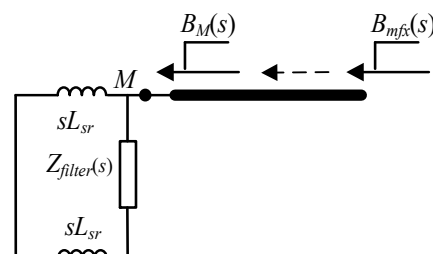
Figure 5. Diagram of TW propagation.

The process satisfies the following frequency domain relationship:

$$\begin{aligned} B_{mx}(s) &= \mathrm{e}^{-\gamma_k L}B_{mfx}(s) \\ \gamma_k(s) &= \sqrt{(R(\omega) + j\omega L(\omega))(G(\omega) + j\omega C(\omega))} \end{aligned} \quad (x = 1,2) \tag{10}$$

where $R(\omega)$, $L(\omega)$, $C(\omega)$ and $G(\omega)$ are the resistance, inductance, capacitance and conductivity of the transmission line per unit length, respectively, and L is the length of line propagation. B_{mfx} is the initial traveling wave at the fault point, B_{mx} is the reverse traveling wave transmitted from the fault point to the measurement point M, and $e^{-\gamma kL}$ represents the transmission formula of the fault traveling wave.

The amplitude–frequency characteristics of the line transfer function are shown in Figure 6.
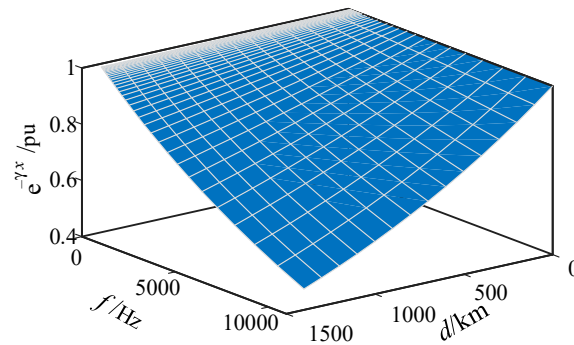

Figure 6. Amplitude–frequency characteristics of the line transmission function.

It can be seen from Figure 6 that the transfer function $e^{-\gamma L}$ of the line increases with the increase in frequency and distance; the high-frequency component and the length of the line will cause serious attenuation of the voltage and current traveling waves at the measuring point. Therefore, when the fault occurs in a long-distance line, it will affect the protection sensitivity that uses only high-frequency components.

2.2.2. The Reflection and Refraction of Traveling Waves

Refraction and reflection occur when the fault TW reaches the node with discontinuous wave impedance, as shown in Figure 7. Considering only the forward TW, the discontinuity of surge impedance is mainly at the outlet of each converter station.
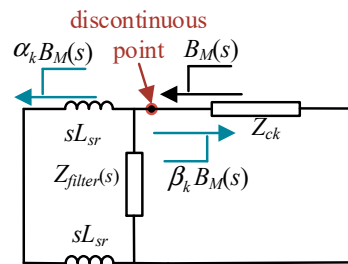
Figure 7. Refraction and reflection of the TW.

According to the Peterson principle, α_k and β_k are the refractive coefficient and the reflection coefficient, respectively:

$$\begin{cases} \alpha_k(s) = \dfrac{2(2sL_{sr}//Z_{filter}(s))}{2sL_{sr}//Z_{filter}(s)+Z_{ck}(s)} \\ \beta_k(s) = \dfrac{2sL_{sr}//Z_{filter}(s)-Z_{ck}(s)}{2sL_{sr}//Z_{filter}(s)+Z_{ck}(s)} \end{cases} (k=l,e). \tag{11}$$

According to the refraction and reflection principles of TWs, the first TW at M is the superposition of the incident wave and the reflected wave. Therefore, the first TW of the voltage and current for f_x (x = 1,2) at M are shown in (12).

$$\begin{cases} U_{Mfxk}(s)= (1+\beta_k)e^{-\gamma L}U_{mfxk}(s) \\ I_{Mfxk}(s) = U_{Mfxk}(s)/Z_{ck}(s) \end{cases} \tag{12}$$

Taken together, the frequency domain power for f_x (x = 1,2,3) at M near the rectifier station are as follows:

$$P_{Mf1k}(s) = U_{Mf1k}(s)I_{Mf1k}(s) = -\frac{2((1+\beta_k)e^{-\gamma_k L})^2 U_0{}^2(Z_{f1k}(s))^2}{s^2(Z_{f1l}(s) + Z_{f1e}(s) + 2R_{f1})^2 Z_{ck}(s)} \tag{13}$$

$$P_{Mf2k}(s) = U_{Mf2k}(s)I_{Mf2k}(s) = -\frac{2((1+\beta_k)e^{-\gamma_k L})^2 U_0{}^2(Z_{f2k}(s)\lambda_u)^2}{s^2(Z_{f2l}(s) + Z_{f2e}(s) + 2R_{f2})^2 Z_{ck}(s)} \tag{14}$$

$$P_{Mf3}(s) = U_{Mf3}(s)I_{Mf3}(s) = \frac{2U_0{}^2(Z_{f3k}(s)\lambda_u)^2}{s^2(Z_{f3l}(s) + Z_{f3e}(s) + 2R_{f3})^2 Z_{ck}(s)} \tag{15}$$

Comparing (8)–(9) and (14)–(15) shows that the frequency domain power retains the polarity of the current. For the FF, the power value is negative, and for the RF, it is positive. Hence, the power polarity can be used to effectively identify external faults on the rectifier side.

2.2.3. Influence of Fault Resistance

According to (13)–(14), the frequency domain is inversely proportional to the square of the fault resistance, meaning that it is more affected by fault resistance than by voltage and current. In the worst-case scenario, $R_{f2} = 0\ \Omega$. By changing the value of the fault resistance R_{f1}, the $G_P(j\omega)$ curves at different frequencies and different R_{f1} values can be obtained, as shown in Figure 8.
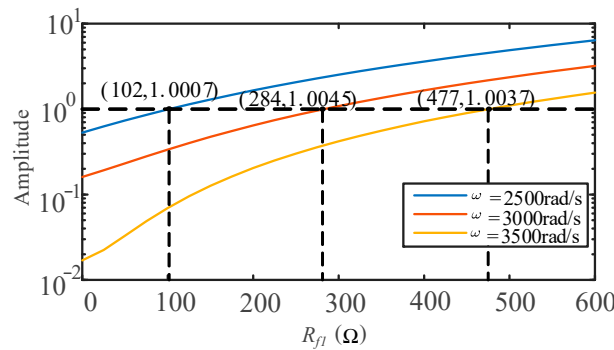
Figure 8. $|G_P(j\omega)|$ at different frequencies and different R_{f1} values ($R_{f2} = 0$).

$G_P(j\omega) = P_{f2}(j\omega)/P_{f1}(j\omega)$, which indicates the ratio of the transient frequency of faults outside the zone to the transient frequency of faults inside the zone. It can be seen from Figure 8:

(1) In the same frequency band, as R_{f1} increases, $P_{f1}(j\omega)$ decreases, resulting in $|G_P(j\omega)|$ rapidly increasing; that is, the $G_P(j\omega)$ characteristics are greatly affected by the transition resistance.

(2) At the same transition resistor, as the frequency increases, $|G_P(j\omega)|$ decreases, indicating that in the high-frequency band, the fault protection method based on frequency extraction can better detect internal and external faults.

Therefore, the protection scheme based on frequency extraction can identify low-resistance faults, but when a high-impedance grounding fault occurs in the DC line, this method is no longer applicable, and theoretically it is impossible to distinguish between internal and external faults based on the power in the frequency domain.

3. Ratio Characteristics of the Frequency Domain Power at Different Frequencies

Based on the above analysis, only the frequency domain power of a certain frequency (frequency band) is greatly affected by the fault resistance. To weaken this influence, a

quantitative index P_{ratio} can be constructed, which is defined as the ratio of the frequency domain power values at different frequencies. We suppose that two different frequencies are ω_1 and ω_2, and that $\omega_1 > \omega_2$. $U_f(j\omega)$ is the step signal. The ratios P_{ratio1} and P_{ratio2} can be obtained under internal and external faults, respectively, as follows:

$$P_{ratio1} = P_{f1}(j\omega_1)/P_{f1}(j\omega_2); P_{ratio2} = P_{f2}(j\omega_1)/P_{f2}(j\omega_2) \tag{16}$$

The line wave impedance also changes with the frequency; therefore, it is necessary to consider the relationship between the line wave impedance and the frequency and draw the waveform of the line wave impedance with frequency according to Equation (10), as shown in Figure 9.
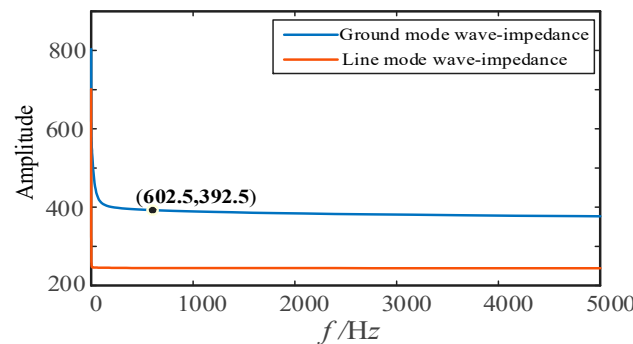

Figure 9. Wave impedance of DC line.

As can be seen from Figure 9, the line wave impedance changes very little with frequency in the high-frequency band and can be approximated into a constant in the high-frequency band. In the same way, it can be seen from Figure 9 that the linear mode wave impedance changes little with frequency compared with the ground mode wave impedance, so the linear mode component is considered for analysis and discussion.

Therefore, the expressions of P_{ratio1} and P_{ratio2} are as follows:

$$
\begin{aligned}
P_{ratio1} &= U_{Mf1}(j\omega_1)I_{Mf1}(j\omega_1)/U_{Mf1}(j\omega_2)I_{Mf1}(j\omega_2) \\
&\approx \omega_2^2(1+\beta(j\omega_1))^2/\omega_1^2(1+\beta(j\omega_2))^2 \\
&= \frac{2Z_{filter}(j\omega_2)j\omega_2 L_{sr}+\left(2j\omega_2 L_{sr}+Z_{filter}(j\omega_2)\right)Z_{c1}}{2Z_{filter}(j\omega_1)j\omega_1 L_{sr}+\left(2j\omega_1 L_{sr}+Z_{filter}(j\omega_1)\right)Z_{c1}}
\end{aligned}
\tag{17}
$$

$$
\begin{aligned}
P_{ratio2} &= U_{Mf2}(j\omega_1)I_{Mf2}(j\omega_1)/U_{Mf2}(j\omega_2)I_{Mf2}(j\omega_2) \\
&\approx \omega_2^2\lambda_u(\omega_1)^2(1+\beta(\omega_1))^2/\omega_1^2\lambda_u(\omega_2)^2(1+\beta(\omega_2))^2 \\
&= P_{ratio1}(j\omega_2 L_{sr}+Z_{c1})^2/(j\omega_1 L_{sr}+Z_{c1})^2
\end{aligned}
\tag{18}
$$

As shown in (17) and (18), P_{ratio1} and P_{ratio2} are only related to the frequency, current-limiting reactance and wave impedance, all of which are basically not affected by the fault resistance.

Letting $|G_{Pratio}| = P_{ratio1}/P_{ratio2}$, we can obtain the following:

$$|G_{Pratio}| = \frac{P_{ratio2}}{P_{ratio1}} \approx \frac{(j\omega_2 L_{sr}+Z_{c1})^2}{(j\omega_1 L_{sr}+Z_{c1})^2} \tag{19}$$

Substituting the model project parameters of the Yun–Guang UHVDC and taking $\omega_2 = 600$ rad/s, the $|G_{Pratio}|$ curves at different frequencies ω_1 and fault resistances R_{f1} can be obtained, as shown in Figure 10.
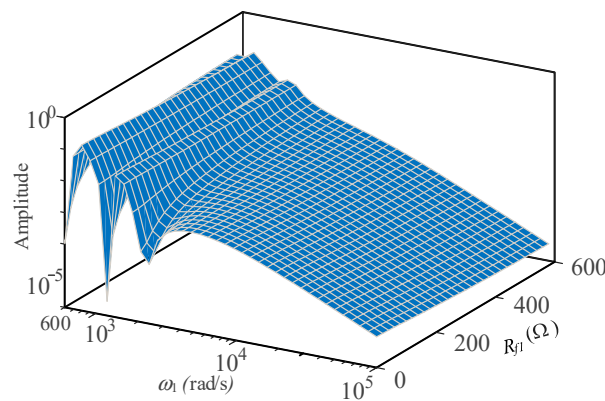
Figure 10. $|G_{Pratio}|$ at different R_{f1} and ω_1.

As can be seen from Figure 10:

(1) In the case of $\omega_1 > \omega_2 = 600\,\text{rad}/\text{s}$, regardless of the transition resistance and frequency ω_1, $G_{Pratio} < 1$, $P_{ratio1} < P_{ratio2}$.

(2) As ω_1 gradually increases, $|G_{Pratio}|$ also further decreases, while $|G_{Pratio}|$ denotes P_{ratio2}/P_{ratio1}, so the difference between the quantitative indicators P_{ratio1} and P_{ratio2} is more obvious, which further amplifies the difference between internal and external faults.

(3) In the same way, when ω_1 is fixed, as the transition resistance R_{f1} gradually increases, the value of $|G_{Pratio}|$ changes slightly, indicating that the ability of $|G_{Pratio}|$ to identify internal and external faults is less affected by the transition resistance ability R_{f1} at different frequencies.

4. Single-Ended Protection Scheme of HVDC Transmission Lines

First, the CP $P_{fi}(t)$ is defined as the convolution of two functions, $U_{fi}(t)$ and $I_{fi}(t)$, in the time domain [24]:

$$P_{fi}(t) = (u_{fi} \times i_{fi})(t) = \int_{t_0}^{t_0+T_s} u_{fi}(t - \tau) i_{fi}(\tau) d\tau \tag{20}$$

where t_0 and T_s are the starting time of the data window and the length of the time window, respectively.

From the convolution theorem, the Laplace transform of function convolution is the product of the function Laplace transform [25]; that is, $U(t)$ and $I(t)$ undergo the Laplace transform to obtain $U(j\omega)$ and $I(j\omega)$ in the frequency domain, and the expression for this relationship is the following:

$$(U \times I)(t) \underset{\text{Equivalent}}{\overset{\text{Laplace transform}}{\longrightarrow}} U(j\omega)I(j\omega) = P_{fi}(s) \tag{21}$$

Therefore, $P_{fi}(t)$ is the CP and $P_{fi}(s)$ is the CP in the frequency domain.

Specifically, the CP represents the application of voltage as an input quantity to all current points within T_s, and is generated by varying the voltage quantity on the current. The convolution operation convolves the input data and can be regarded as a weighted summation, whereas the result of the convolution is the feature extraction and the amplification of the fault characteristics. The convolution calculation process is shown in Figure 11. The input signal u(t) is regarded as a discrete sequence u(n) = {u$_1$, u$_2$, u$_3$, ..., u$_n$}; i(t) is regarded as a discrete sequence i(n) = {i$_1$, i$_2$, i$_3$, ..., i$_n$}.

It can be seen from Figure 11 that the convolution power result under the sampling point can be obtained by adding each column in Figure 11, and the convolution result presents the arrangement results from small to large and then large to small, and the discrete signal convolution power solution is obtained through the convolution calculation process of Figure 11:

$$P_a(X) = \sum_{i=1}^{N} U_a(i) I_a(X - i + 1) \ (a = p, n) \tag{22}$$

where P_a is the CP; X is the Xth sampling point; and N is the total number of sampling points, which reflects the length of the time window. N is calculated as follows, where f_s is the sampling frequency:

$$N = T_s f_s \tag{23}$$

$u(X)$ \ X	1	2	3	4	n	2n−2	n+n−1
u_1	$u_1 i_1$	$u_1 i_2$	$u_1 i_3$	$u_1 i_4$	$u_1 i_n$	0	0
u_2	0	$u_2 i_1$	$u_2 i_2$	$u_2 i_3$	$u_2 i_{n-1}$	0	0
u_3	0	0	$u_3 i_1$	$u_3 i_2$	$u_3 i_{n-2}$	0	0
u_4	0	0	0	$u_4 i_1$	$u_4 i_{n-3}$	0	0
$\vdots$	0	0	0	0	$\vdots$	$\vdots$	$\vdots$
u_n	0	0	0	0	$u_n i_1$	$u_{n-1} i_1$	$u_n i_1$

Figure 11. Specific convolution calculation process.

In fact, because the TW is a nonstationary time signal, its spectrum distribution is related to the time window. For different time windows, the spectrum distribution is not consistent. Therefore, the spectrum distribution of the CP is also affected by the time window. From the perspective of signal processing, when the sampling frequency is fixed, the length of the time window reflects different frequency resolutions. According to the Shannon sampling theorem, the fault information also contains many harmonic component frequencies, except the fundamental frequency signal in the long and short windows, but the frequency resolution of each time window is inversely proportional to the length of the time window. Taking the sampling frequency of 10 kHz as an example, when the short window is 1 ms, the minimum frequency interval on the frequency axis is 1000 Hz, whereas when the long window is 3 ms, the minimum frequency interval is 333.33 Hz. Therefore, it is clear that compared with that of the short window, the frequency component of the long window is greater [26]. In detail, the fault frequency information in the short window can be regarded as high-frequency information. Similarly, the long window can be regarded as the wide band of low-frequency and high-frequency information.

The single-ended protection scheme for HVDC transmission lines is described in the following sections.

4.1. Starting Criterion

When a fault occurs in the line, the pole line voltage suddenly changes. Therefore, the variation in polar line voltage ΔU_a can be used as the starting criterion of the protection:

$$\sum_{j=0,1,2} |\Delta U_a(j + i) - \Delta U_a(j + i - 1)| > k_v U_{ref} \ (a = p, n) \tag{24}$$

where U_{ref} is the rated voltage and a represents the fault pole. To avoid the influence of steady-state voltage fluctuations, k_v is the voltage fluctuation coefficient and is taken as 0.08.

4.2. Fault Identification Criteria of the Internal and External Faults

The maximum value of the CP sequence under long and short windows is selected as the characteristic quantity.

4.2.1. Main Criterion 1

Main criterion 1 adopts the CP with a short window of T_1. The main function of the criterion is to quickly identify serious faults, including the metallic and low-resistance faults. Main criterion 1 is given as follows:

$$P_{aT1max} > P_{aT1.set} = k_{rel.1}P_{f2T1max}(a = p, n) \tag{25}$$

where $P_{aT1max} = max(|P_{aT1}|)$, and P_{aT1} is the discrete CP value obtained by convolution of the voltage and current within T_1, taken as 1 ms. $P_{f2T1max}$ represents the metal external fault inverter side within T_1; $k_{rel.1}$ is the reliability coefficient, taken as 1.5.

4.2.2. Main Criterion 2

Main criterion 1 is based on the CP with a short window, and has the advantages of simplification and rapid tripping, but its sensitivity is reduced with increasing fault resistance. To address this issue, a criterion composed of the CP ratio (R_a) at different frequencies is added to assist in identifying high-resistance faults. Main criterion 2 is the following:

$$R_a > R_{a.set} = k_{rel.2}R_{f2a}(a = p, n) \tag{26}$$

where $\begin{cases} R_a = P_{aT1max}/P_{aT2max} \\ P_{aT2max} = max(|P_{aT2}|) \end{cases}$, $R_{a.set}$ represents the setting value, R_{f2a} is the ratio of long- and short-window CPs of the metal external fault inverter side, P_{aT2} is the discrete CP value obtained by convolution of the voltage and current within T_2, taken as 3 ms, and $k_{rel.2}$ is the reliability coefficient, taken as 2.

Compared to main criterion 1, the above criterion requires waiting for a long window and increasing the number of calculations. However, when a high-resistance fault occurs, the rising speed of the fault current is relatively slow, and the system allows a longer response time for the protection action.

4.3. Fault Direction Identification Criterion

As mentioned in Section 2, the polarity of the CP can be used to distinguish the RF and FF, so the fault direction can be identified by the polarity of the short-window CP, including Δ_{th1} as the threshold value:

$$\begin{cases} A_1 = min(P_{aT1}) > \Delta_{th1} & RF \\ A_1 = min(P_{aT1}) < -\Delta_{th1} & FF \end{cases} \tag{27}$$

4.4. Fault Pole Selection Identification Criterion

The coupling strength between DC lines is related to frequency. In the high-frequency band, the coupling strength is relatively large, so the high-frequency components of the sound pole and fault pole are very similar. However, in the low-frequency band, the coupling strength is weak, so the low-frequency component of the fault pole is more significant than that of the sound pole. Therefore, a pole selection criterion based on a low-frequency CP under a long window can be constructed as follows:

$$\begin{cases} \frac{P_{pT2max}}{P_{nT2max}} > \Delta_{th2} & PGF \\ \frac{P_{pT2max}}{P_{nT2max}} < \frac{1}{\Delta_{th2}} & NGF \\ \Delta_{th2} > \frac{P_{pT2max}}{P_{nT2max}} > \frac{1}{\Delta_{th2}} & PPF \end{cases} \tag{28}$$

where Δ_{th2} is the threshold value and $k_{rel.3}$ is the reliability coefficient, which is 1.5. The rectifier station acts according to the protection result after fault identification, and then the DC system enters the fault isolation and recovery phase. PGF is a positive ground fault, NGF is a negative ground fault, and PPF is a fault between poles.

In summary, this study designed a single-ended protection scheme that has both advantages with the CP ratios of short and long windows. The specific flow chart is shown in Figure 12, which is composed of main criterion 1 and main criterion 2.
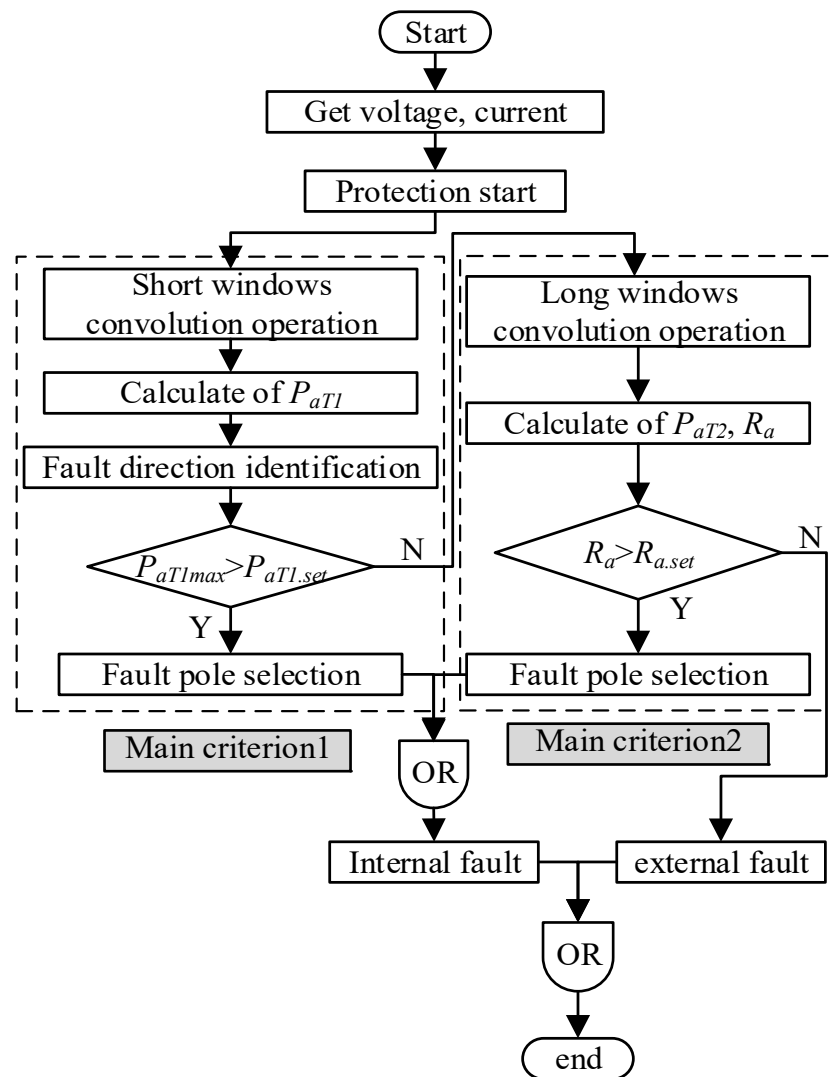
```
                          ┌─────────┐
                          │  Start  │
                          └─────────┘
                               │
                    ┌──────────────────────┐
                    │  Get voltage, current │
                    └──────────────────────┘
                               │
                    ┌──────────────────────┐
                    │    Protection start   │
                    └──────────────────────┘
```

Short windows convolution operation

Calculate of P_{aT1}

Fault direction identification

$P_{aT1max} > P_{aT1.set}$ N

Y

Fault pole selection

Main criterion1

Long windows convolution operation

Calculate of P_{aT2}, R_a

$R_a > R_{a.set}$ N

Y

Fault pole selection

Main criterion2

OR

Internal fault

external fault

OR

end

Figure 12. Flowchart of a novel single-ended protection scheme based on the CP ratio.

5. Case Analysis

A ±800 kV UHVDC transmission system model was established in PSCAD/EMTDC with respect to the parameters of the Yunnan to Guangdong UHVDC transmission project. The specific model parameters are shown in Table 1. The structures of the DC line are depicted in Figure 13. The sampling frequency is 10 kHz. The time windows of the CPs are 1 ms and 3 ms, so the numbers of sampling points N are 10 and 30, respectively. The protection algorithm was written in MATLAB software. According to the setting principle and simulation results, the criterion-setting value of the protection scheme is shown in Table 2. The steps in the following sections are used to verify the action of protection under different faults.

Table 1. Model parameters.

Parameter	Rectifier Side	Inverter Side
Rated power	5000 MW	5000 MW
Rated DC current(I_0)	3125 A	3125 A
Rated DC voltage(U_0)	±800 kV	±800 kV
Boundary element (L_{sr})	0.15 H	0.15 H
Filter	C_{f1} = 1.2 μF C_{f2} = 2.824 μF C_{f3} = 2.647 μF L_{f1} = 9.345 mH L_{f2} = 15.919 mH L_{f3} = 4.6556 mH	
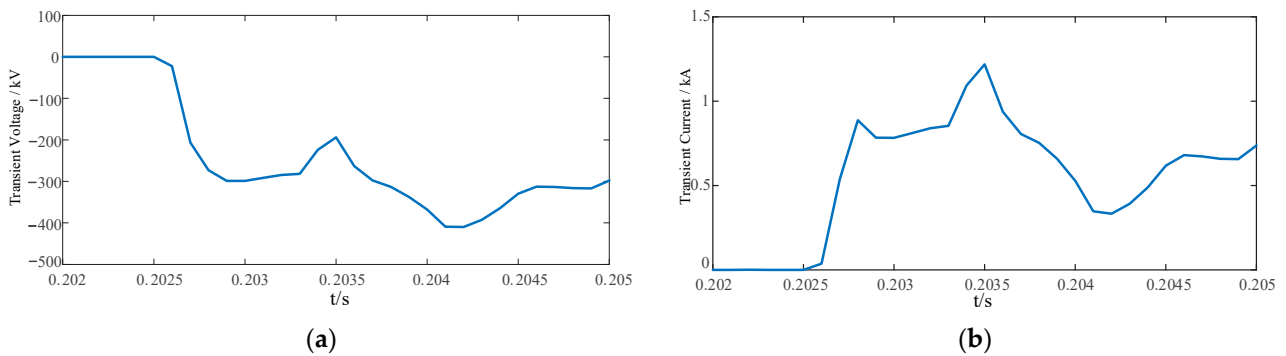
Figure 13. Transient current under internal faults. (**a**) Transient voltage under internal faults. (**b**) Transient current under internal faults.

Table 2. Setting value of protection criterion.

Criterion	Δ_{th1}	Δ_{th2}	$P_{pT1.set}$	R_P
Setting value	20	1	900	0.08

5.1. Identification of Internal and External Faults

The fault occurs at t = 0.2 s, and when a PGF occurs at point f_1 (internal fault), the fault voltage and fault current at the boundary measurement point after the fault are shown in Figure 13.

The transient convolution power graphs of the long and short windows calculated with Equations (20)–(22) in the case of internal faults are shown in Figure 14.
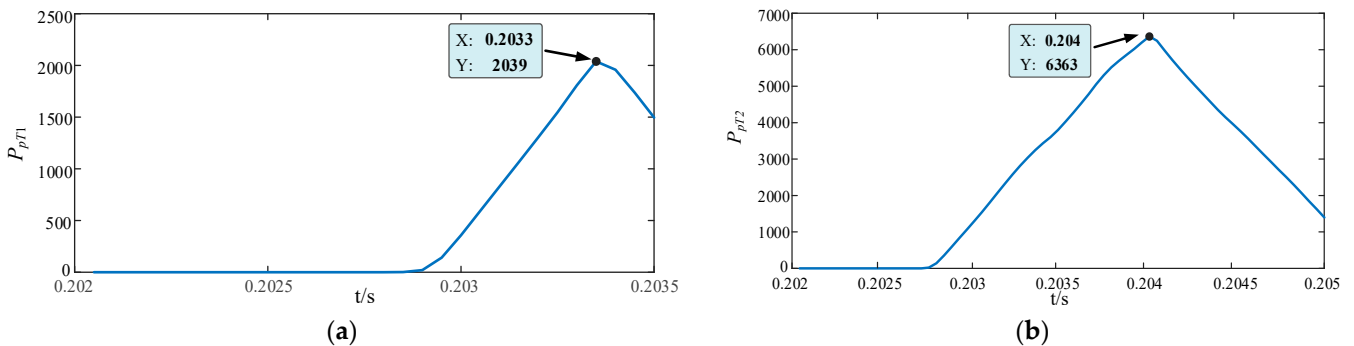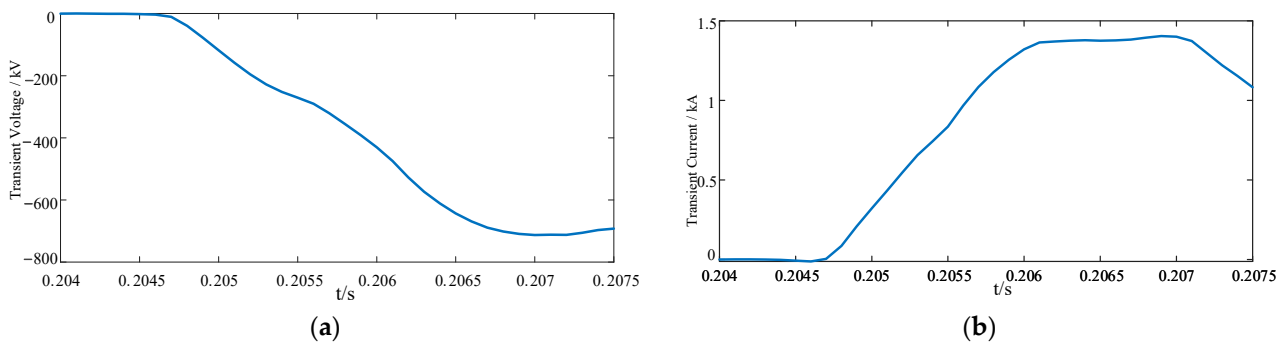

Figure 14. Long and short window transient convolutional power. (**a**) Short time window transient convolutional power. (**b**) Long time window transient convolutional power.

As shown in Figure 14, $P_{\text{pT1\_MAX}}$ = 2039 > $P_{\text{pT1\_set}}$ = 900 in main criterion I; similarly, the ratio of the convolution power calculated with main criterion II according to Formulas (25) and (26), is P_{ratio} = 0.32 > R_p = 0.08. Therefore, the protection is determined as an internal fault.

When a PGF occurs at point f_2 (external fault), the fault voltage and fault current at the boundary measurement point after the fault are shown in Figure 15.

The transient convolution power graphs of the fault for long and short windows calculated using Equations (20)–(22) during external faults are shown in Figure 16.

From Figure 16, it can be seen that P_{pT1_max} = 681 < P_{pT1_set} = 900 for main criterion I; similarly, it can be seen that the ratio of convolution power calculated via main criterion II according to Formulas (25) and (26), is P_{ratio} = 0.045 < R_p = 0.08. Therefore, the protection is determined as an external fault.

Figure 15. Transient current under internal faults. (**a**) Transient voltage under internal faults. (**b**) Transient current under internal faults.
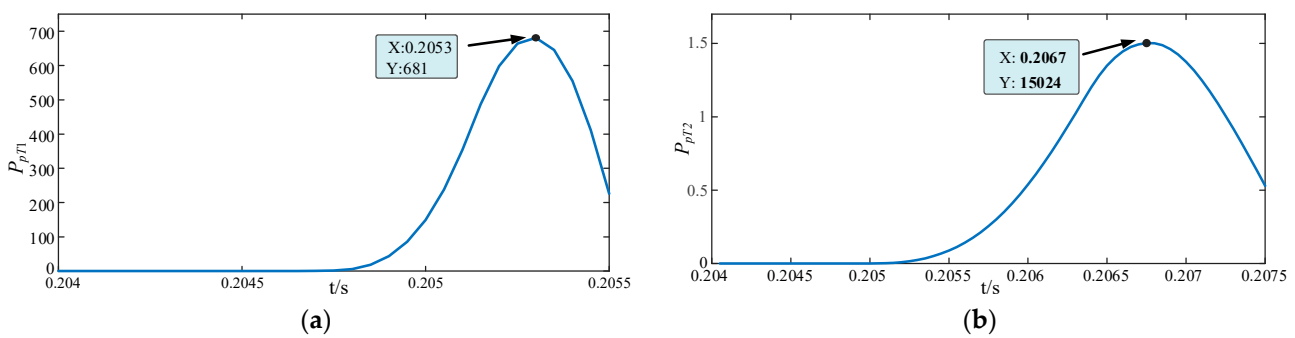
Figure 16. Long- and short-window transient convolutional power. (**a**) Short-time-window transient convolutional power. (**b**) Long-time-window transient convolutional power.

To verify the accuracy and applicability of the protection scheme, the simulation was set to have high-resistance faults at every 200 km interval of the lines, with their resistances varying from 0 to 600 Ω. Considering the most serious situation, f_2 and f_3 were set as metallic ground faults in the later analysis. Since the positive and negative poles are symmetrical, only the positive fault is discussed here. In the table below, $\sqrt{}$ represents the protection action; conversely, $\times$ represents no action. Limited by the article space, only some fault point simulation results are shown here. The simulation test results are shown in Table 3.

Table 3 shows the following:

(1) In the case of low-impedance grounding faults (internal faults), the maximum value of the high-frequency convolution power of each fault type, $P_{pT1\max}$, is much greater than that of P_{pT1set}, and the A1 value is obtained by the calculation using Equation (27) in order to determine the fault direction; therefore, main criterion 1 in the proposed protection scheme can quickly and reliably identify the low-impedance grounding faults in the region.

(2) As shown in the shaded font in Table 3, when the transition resistance is set at a distance of 1414 km from the protection installation to a fault of 600 Ω, $P_{pT1\max}$ is equal to 882, which is less than the setting value P_{pT1set}, which may cause the effect of rejection.

(3) In order to prevent the rejection phenomenon when the high-impedance grounding fault is made, this study proposes to use main criterion 2 to identify the high-impedance grounding fault inside and outside the region. From the observations in the table, it can be seen that the P_{ratio} under the internal fault (f_1) is greater than that under the external fault (f_2), and the value of the P_{ratio} is still greater than that of the metal fault outside the area on the inverter side, even if the transition resistance is 600 Ω, which ensures the identification of the high-impedance fault in the area via main criterion 2.

Table 3. Fault identification results for internal and external faults.

| Fault Distance/km	Fault Type	Transition Resistance/Ω	Fault Direction	A_1	P_{pT2max}	P_{pT1max}	R_P	Action of Main Criteria 1 and 2
0	PGF	0	FF	−5916	18,743.6	5915.6	0.316	(1√, 2√)
		160	FF	−1354.8	4235.4	1354.8	0.320	(1√, 2√)
		200	FF	−1051	3301.7	1050.7	0.318	(1√, 2×)
		400	FF	−396	1258.2	395.9	0.315	(1×, 2√)
		600	FF	−196	623.4	196.1	0.314	(1×, 2√)
	PPF	0	FF	−30,961	88,281.1	30,960.9	0.350	(1√, 2√)
		600	FF	−2899	9027.5	2898.8	0.321	(1√, 2√)
400	PGF	0	FF	−3871	15,410.5	3870.6	0.251	(1√, 2√)
		160	FF	−1111.5	3933.8	1111.5	0.283	(1√, 2√)
		200	FF	−876	3087.5	875.6	0.284	(1×, 2√)
		400	FF	−353	1212.4	352.7	0.291	(1×, 2√)
		600	FF	−186	615.9	186.3	0.303	(1×, 2√)
	PPF	0	FF	−27,464	116,074.2	27,464.2	0.237	(1√, 2√)
		600	FF	−2482	9400.4	2481.7	0.264	(1√, 2√)
800	PGF	0	FF	−3802	14,702.4	3801.7	0.259	(1√, 2√)
		160	FF	−952.9	3736.3	952.9	0.255	(1√, 2√)
		200	FF	−752	2936.1	751.9	0.256	(1×, 2√)
		400	FF	−358	1194.2	357.8	0.300	(1×, 2√)
		600	FF	−190	616.0	190.0	0.308	(1×, 2√)
	PPF	0	FF	−22,507	105,594.7	22,506.7	0.213	(1√, 2√)
		600	FF	−2227	9245.6	2227.2	0.241	(1√, 2√)
1418 (f_1)	PGF	0	FF	−3795	17,621.5	3795.1	0.215	(1√, 2√)
		160	FF	−882.0	3985.7	882.0	0.221	(1×, 2√)
		200	FF	−719	3691.0	718.8	0.195	(1×, 2√)
		400	FF	−283	1520.2	283.1	0.186	(1×, 2√)
		600	FF	−167	808.6	166.5	0.206	(1×, 2√)
	PPF	0	FF	−16,061	15,331.7	16,061.0	0.179	(1√, 2√)
		600	FF	−1918	614.0	1918.3	0.178	(1√, 2√)
f_2	PGF	0	FF	−601	15,429.1	600.9	0.039	(1×, 2×)
f_3	PGF	0	RF	0.00345	/	2235.11	/	/

5.2. Faulty Pole Selection

When the protection method in this research determines that the fault is an internal fault, it is necessary to further select the fault pole selection criterion for the fault in the region. The waveforms of the long window convolution power P_{pT2} for a PGF, NGF and PPF occurring at point f_1 are shown in Figure 17.

As shown in Figure 17:

(1) When a positive pole fault occurs in the system, the ratio of transient convolution power between the positive and negative poles on the rectifier side is much greater than 1.5.

(2) When a negative pole fault occurs in the system, the ratio of transient convolution power between the positive and negative poles on the rectifier side is less than 0.67.

(3) When an interpole fault occurs in the system, the ratio of transient convolution power between the positive and negative poles on the rectifier side is between 0.67 and 1.5.

At the 400 km location in the DC line, the NGF and PGF are applied under different resistances, and the corresponding waveform of P_{pT2} with a long window is shown in Figure 18.

Figure 18 shows that although the CP with a long window decreases with increasing fault resistance, the waveform of P_{pT2} of the PGF is always above that of the NGF, within 600 Ω. Therefore, the CP with a long window can be used to identify the faulty pole, which is consistent with the description in Section 4. In the actual criterion, the fault pole is judged by calculating the ratio (P_{pT2max}/P_{nT2max}). The simulation test results of specific fault pole selection are shown in Table 4.
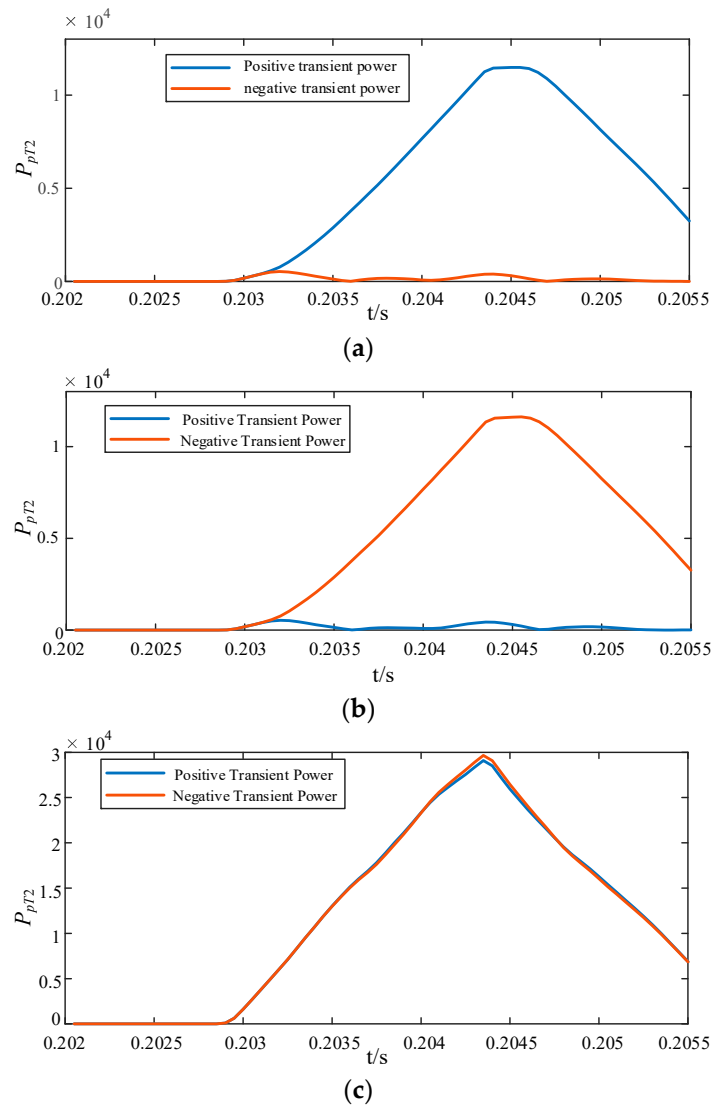
Figure 17. Convolutional power under different fault types. (**a**) Convolutional power during positive pole fault. (**b**) Convolutional power during negative pole fault. (**c**) Convolutional power during interpole faults.
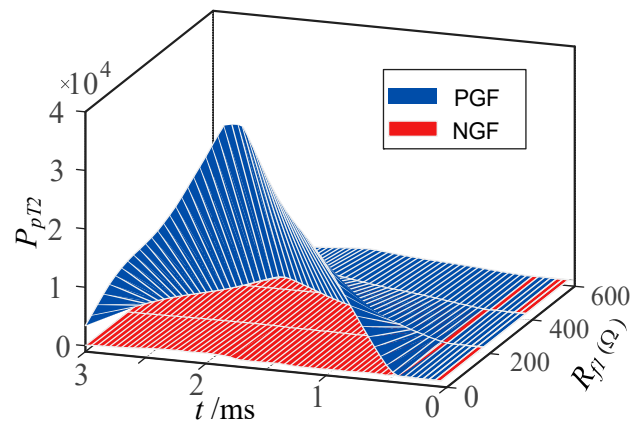
Figure 18. P_{pT2} in case of a PGF and NGF.

Table 4. Faulty pole selection results.

Fault Type	Resistance/Ω	P_{pT2max}/P_{nT2max}
400 km PGF	0	64.710
	200	65.547
	400	52.141
	600	43.037
400 km NGF	0	0.0181
	200	0.0220
	400	0.0208
	600	0.0228
400 km PPG	0	0.9989
	200	0.9988
	400	0.9990
	600	0.9991

Table 4 shows that in various fault conditions, the proposed criterion can reliably distinguish the fault pole.

5.3. Adaptability Analysis of the Noise Interference

In practical engineering, the line may encounter noise interference, which affects the reliability of the line protection action. After sampling interference signals such as noise, the obtained digital signal contains more high-frequency components, which affect the action performance of the criterion based on transient variation. To verify the anti-interference ability of the protection scheme, Gaussian white noise based on the actual signal power value was added to the voltage and current measured at M_1, and the signal-to-noise ratio (SNR) was 40 dB. Taking the middle of the line as an example, the specific simulation results of the scheme proposed in [26] and the scheme proposed in this research are shown under severe Gaussian white noise interference in Table 5.

Table 5. Action performance of main criteria 1 and 2 after adding noise.

Fault Distance	Fault Resistance	Noisy P_{pT1max}	Noisy R_P	Criterion Action	No-Noise TTV	Noisy TTV
600 km	0 Ω	3694.5	0.254	$(1\checkmark, 2\checkmark)$	0.413	0.396
	200 Ω	768.5	0.267	$(1\times, 2\checkmark)$	0.357	0.365
	400 Ω	280.9	0.253	$(1\times, 2\checkmark)$	0.383	0.435
	600 Ω	158.2	0.272	$(1\times, 2\checkmark)$	0.318	0.350
f_2	0 Ω	851.7	0.053	$(1\times, 2\times)$	0.168	0.265

The simulation results in Table 5 show that the protection criteria proposed in this study can withstand 40 dB of Gaussian white noise and maintain the original performance. However, the protection scheme based on the time-domain transient voltage in [22] is vulnerable to Gaussian white noise, especially in the case of external faults. It is necessary to recalculate the setting value to avoid protection misoperation. Therefore, the proposed protection scheme has a better ability to resist noise interference.

5.4. Adaptability Analysis of the Boundary Element

When the high-frequency component passes through the boundary element, such as a smoothing reactor, it is greatly attenuated, and the attenuation degree of the high-frequency component is different for smoothing reactors with different values, which affects the adaptability of the protection principle. Therefore, the simulation verifies the adaptability

of the method to smoothing reactors with different values when a fault occurs. The specific simulation results are shown in Table 6.

Table 6. Results under different values of smoothing reactor.

| Fault Distance	Fault Resistance	L_{sr} /H	P_{pT2max}	P_{pT1max}	R_P	Protection Margin $(P_{pT1max}/P_{pT1.set}, R_P/R_{P.set})$
0 km	0 Ω	0.15	18,743	5915.6	0.316	(6.572, 3.950)
		0.10	2215	6682.4	0.302	(4.330, 2.649)
		0.05	26,628	7505.4	0.282	(2.414, 1.270)
	600 Ω	0.15	623.4	196.1	0.314	(0.218, 3.925)
		0.10	587.0	185.3	0.316	(0.120, 2.772)
		0.05	567.2	176.0	0.310	(0.056, 1.396)
1418 km (f_1)	0 Ω	0.15	17,621	3795.1	0.286	(4.217, 2.687)
		0.10	17,145	3175.6	0.185	(2.058, 1.614)
		0.05	18,172	4062.3	0.224	(1.307, 1.010)
	600 Ω	0.15	808.6	166.5	0.290	(0.185, 2.575)
		0.10	698.6	132.2	0.292	(0.128, 2.561)
		0.05	663.7	138.1	0.295	(0.044, 1.329)
f_2	0 Ω	0.15	15,429	600.9	0.039	/
		0.10	18,008	1028.8	0.057	/
		0.05	18,684	2072.7	0.111	/

As shown in Table 6, with the reduction in the smoothing reactor value, the CP value of the short window of an external fault continues to increase, resulting in a reduction in the discrimination degree of the out-of-area faults. Thus, protection criteria based on high frequencies, such as main criterion 1, are greatly affected by boundary elements. However, different smoothing reactor values have little effect on the action performance of main criterion 2 proposed in this study. When $L_{sr} > 50$ mH and the fault resistance is 600 Ω, main criterion 2 still has a sufficient margin for identifying faults. Therefore, the proposed protection scheme is also suitable for HVDC transmission systems with weak boundary characteristics, which are easy to implement and have good universality.

5.5. Comparison Studies

(1)   Time-domain method:

Using the rate of change of DC voltage (ROCOV)-based fault protection scheme proposed in reference [6], the superiority of the proposed scheme is verified through simulation comparison.

Set a positive grounding fault with a transition resistance of 400 Ω at f_1 (internal fault), and a metallic grounding fault (external fault) at f_2. The ROCOV waveform is shown in Figure 19.
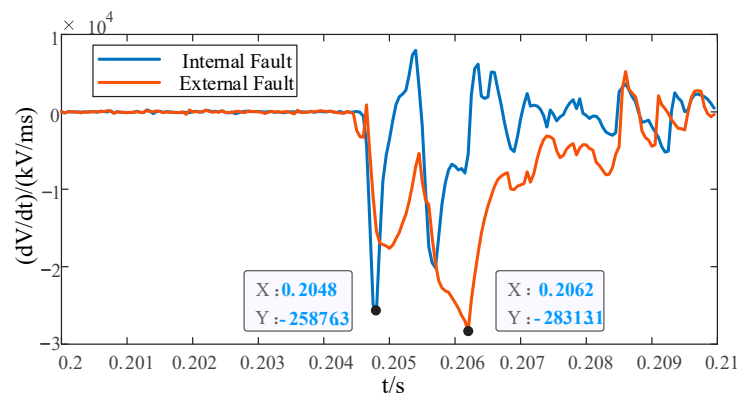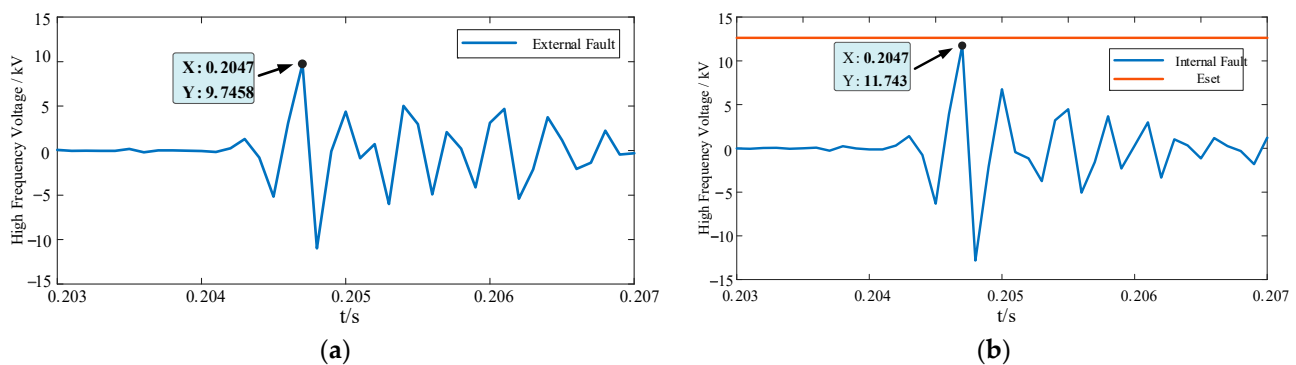

Figure 19. ROCOV under internal and external faults.

As shown in Figure 18, the ROCOV at f_2 is greater than that at f_1, and the ROCOV's ability to withstand transition resistance is less than 400 Ω. However, the protection scheme proposed in this research has a resistance to transition resistance of 600 Ω. Therefore, using ROCOV alone cannot identify high-resistance faults.

(2)   Frequency domain method

A protection scheme based on wavelet transforms for measuring high-frequency component values of point voltages was proposed in reference [12]. Similarly, a positive grounding fault with a transition resistance of 500 Ω was set at f_1 under a weak boundary (L_{dc} = 50 mH) (internal fault), and a metallic grounding fault was set at f_2 (external fault). The transient high-frequency voltage components obtained through wavelet transforms are shown in Figure 20.

Figure 20. High-Frequency Voltage under internal and external faults. (**a**) High-Frequency Voltage under internal faults. (**b**) High-Frequency Voltage under external faults.

By setting the metal grounding fault outside the zone, the maximum transient high-frequency voltage of the most severe external fault is 9.7485. Setting the reliability coefficient K_{rel} = 1.3 can obtain the setting value for internal and external faults in the zone. From Figure 20, the grounding fault with a transition resistance of 500 Ω in the area is less than the set value, so the protection will refuse to operate. As the smoothing reactor of this scheme adopts 50 mH, it is not suitable for weak boundary systems. Meanwhile, as a time–frequency analysis tool, wavelet transform has complex computational principles. And this article uses time-domain convolution power to extract high-frequency signals with a simple principle, and the proposed protection scheme has a resistance to transition resistance of 600 Ω.

6. Conclusions

To resolve the problem of the insufficiency of HVDC transmission systems to withstand fault resistance, a fault characteristic quantity based on the CP was constructed, and a novel single-ended protection scheme based on the CP ratio for HVDC transmission lines was proposed. The results of the mathematical analysis and numerical examples show the following achievements:

(1)   By analyzing the characteristic difference in frequency domain power after DC line fault in detail, a new protection criterion was proposed using the power ratio of different frequencies under long and short windows. The scheme is less affected by transition resistance and fault distance, and the principle of the proposed scheme is simple. It can obtain the frequency domain component of a fault traveling wave without relying on other methods, such as extracting frequency domain information.

(2)   The Yunnan–Guangzhou ±800 kV HVDC project was built to verify the performance of the proposed fault rapid identification scheme. In all cases, it can accurately identify faults, has the identification ability of up to 600 Ω transition resistance, and has low requirements for the sampling frequency of the protection device. Only a 10 kHz

sampling frequency is required to identify faults inside and outside the area. Moreover, when the SNR is greater than 40 dB, noise has little effect on the proposed method.

(3) Compared with other time-domain methods based on measuring point voltage change and frequency domain methods based on wavelet transform extraction, the proposed protection scheme can identify different types of short-circuit faults and has a strong ability to withstand excessive resistance. The proposed protection scheme can also be applied to HVDC transmission systems with weak boundary characteristics.

Future work plans to apply this method to flexible HVDC transmission systems under weak boundaries.

Author Contributions: Conceptualization, G.P., L.C. and J.W.; methodology, G.P., L.C., J.W. and H.J.; validation, H.J., Z.W. and H.L.; formal analysis, G.P., L.C. and J.W.; investigation, G.P., L.C. and J.W.; resources, G.P., L.C. and J.W.; data curation, H.J., Z.W. and H.L.; writing—original draft preparation, G.P., L.C., J.W., H.J., Z.W. and H.L.; writing—review and editing, G.P., L.C., J.W., H.J., Z.W. and H.L. All authors have read and agreed to the published version of the manuscript.

Data Availability Statement: All data generated or analyzed during this study are included in this published article.

Conflicts of Interest: The authors declare no conflict of interest.

References

1. Ma, J.; Liu, C.; Wu, Y. A Pilot Directional Protection Scheme for LCC-HVDC Lines Based on Grounding Resistance. *IEEE Trans. Power Deliv.* **2022**, *37*, 4460–4473. [CrossRef]
2. Chen, Y.; Wen, M.; Wang, Z. A pilot directional protection based on low frequency voltage variable quantity for LCC-HVDC transmission lines. *Int. J. Electr. Power Energy Syst.* **2023**, *145*, 108512. [CrossRef]
3. Zhang, Y.; Li, Y.; Song, J. A New Protection Scheme for HVDC Transmission Lines Based on the Specific Frequency Current of DC Filter. *IEEE Trans. Power Deliv.* **2019**, *34*, 420–429. [CrossRef]
4. Yu, S.; Wang, X.; Zhang, X. A sensitive single-end DC line fault detection method for MMC-HVDC grids using reactor voltage ratio. *Int. J. Electr. Power Energy Syst.* **2023**, *148*, 108953. [CrossRef]
5. Ma, J.; Kang, J.; Zhou, Y.; Cheng, P. A Novel Pilot Protection Scheme for AC Line Connected to LCC-HVDC Inverter Based on Composite-Mode Model. *IEEE Trans. Power Deliv.* **2022**, *37*, 1627–1639. [CrossRef]
6. Liu, Z.; Gao, H.; Luo, S. Non-unit protection for long-distance LCC-HVDC transmission lines based on waveform characteristics of voltage travelling waves. *Int. J. Electr. Power Energy Syst.* **2023**, *150*, 109079. [CrossRef]
7. Rafael, L. One-terminal traveling wave-based transmission line protection for LCC-HVDC systems. *Electr. Power Syst. Res.* **2023**, *223*, 109650.
8. Liu, J.; Lin, S.; Zhong, W.; Liu, L. Improved Identification Method and Fault Current Limiting Strategy for Commutation Failure in LCC-HVDC. *J. Mod. Power Syst. Clean Energy* **2022**, *10*, 1761–1772. [CrossRef]
9. Li, R.; Xu, L.; Yao, L. DC fault detection and location in meshed multi-terminal HVDC systems based on DC reactor voltage change rate. *IEEE Trans. Power Deliv.* **2016**, *32*, 1516–1526. [CrossRef]
10. Sneath, J.; Rajapakse, A. Fault detection and interruption in an earthed HVDC grid using ROCOV and hybrid DC breakers. *IEEE Trans. Power Deliv.* **2016**, *31*, 973–981. [CrossRef]
11. Yang, S.; Xiang, W.; Li, R.; Lu, X.; Zuo, W.; Wen, J. An improved DC fault protection algorithm for MMC HVDC grids based on modal domain analysis. *IEEE J. Emerg. Sel. Top. Power Electron.* **2020**, *8*, 4086–4099. [CrossRef]
12. Zhang, C.; Song, G.; Dong, X. A Novel Traveling Wave Protection Method for DC Transmission Lines Using Current Fitting. *IEEE Trans. Power Deliv.* **2020**, *35*, 2980–2991. [CrossRef]
13. Zhang, C.; Li, Y.; Song, G.; Dong, X. Fast and Sensitive Nonunit Protection Method for HVDC Grids Using Levenberg–Marquardt Algorithm. *IEEE Trans. Ind. Electron.* **2022**, *69*, 9064–9074. [CrossRef]
14. Jia, K.; Chen, M.; Shi, Z.; Chen, C.; Zhao, G.; Bi, T. Single-ended protection scheme of flexible DC transmission line based on concavity and convexity of the current limiting reactor voltage integration. *Power Syst. Technol.* **2021**, *45*, 4498–4505.
15. Yu, X.; Gu, J.; Zhang, X. A non-unit transmission line protection scheme for MMC-HVDC grids based on a novel distance criterion. *Int. J. Electr. Power Energy Syst.* **2023**, *151*, 109151. [CrossRef]
16. Li, B.; Li, Y.; He, J.; Wen, W. A Novel Single-Ended Transient-Voltage-Based Protection Strategy for Flexible DC Grid. *IEEE Trans. Power Deliv.* **2019**, *34*, 1925–1937. [CrossRef]
17. Liu, N.; Li, Y.; Li, S.; Li, T.; Yu, L. A pilot protection for LCC-HVDC transmission lines based on measured surge impedance at tuning frequency. *IEEE Trans. Power Deliv.* **2022**, *37*, 2090–2103. [CrossRef]

18. Dai, Z.; Liu, N.; Zhang, C.; Pan, X.; Wang, J. A pilot protection for HVDC transmission lines based on transient energy ratio of DC filter link. *IEEE Trans. Power Deliv.* **2020**, *35*, 1695–1706. [CrossRef]
19. Shu, H.; Wang, S.; Lei, S. Single-ended protection method for hybrid HVDC transmission line based on transient voltage characteristic frequency band. *Prot. Control. Mod. Power Syst.* **2023**, *26*, 8. [CrossRef]
20. Duan, J.; Li, H.; Lei, Y.; Tuo, L. A novel non-unit transient based boundary protection for HVDC transmission lines using synchrosqueezing wavelet transform. *Int. J. Electr. Power Energy Syst.* **2020**, *115*, 105478. [CrossRef]
21. Zhang, D.; Wu, C.; He, J.; Luo, G. Research on single-ended protection principle of LCC-VSC three-terminal DC transmission line. *Int. J. Electr. Power Energy Syst.* **2022**, *135*, 107512. [CrossRef]
22. Zhang, Y.; Cong, W. An improved single-ended frequency-domain-based fault detection scheme for MMC-HVDC transmission lines. *Int. J. Electr. Power Energy Syst.* **2021**, *125*, 106463. [CrossRef]
23. Psaras, V.; Tzelepis, D.; Vozikis, D.; Adam, G.; Burt, G. Non-unit protection for HVDC grids: An analytical approach for wavelet transform-based schemes. *IEEE Trans. Power Deliv.* **2021**, *36*, 2634–2645. [CrossRef]
24. Ye, D.; Xie, F.; Hao, Z. A novel identification scheme of lightning disturbance in HVDC transmission lines based on CEEMD-HHT. *CPSS Trans. Power Electron.* **2021**, *6*, 145–154. [CrossRef]
25. Wei, D. Novel convolution and correlation theorems for the fractional fourier transform. *Optik* **2016**, *127*, 3669–3675. [CrossRef]
26. Chen, X.; Li, H.; Liang, Y.; Wang, G. A protection scheme for hybrid multi-terminal HVDC networks utilizing a time-domain transient voltage based on fault-blocking converters. *Int. J. Electr. Power Energy Syst.* **2020**, *118*, 105825. [CrossRef]